Li Metal Batteries

Molecular Engineering of Weakly Solvating Dinitrile Electrolytes for Long-Lasting Room-Temperature Lithium Metal Batteries

Chuan Luo, Chunpeng Ning, Xuehai Huang, Panjing Zhang, Liwei Yang, Sijing Wang, Junchen Wang, Yu Wang, Kai Wan, Zi-Hao Guo, Kan Yue,* and Zhenxing Liang*

Abstract: The development of lithium metal batteries (LMBs) relies on advanced solid-state electrolytes. Solid-state polymer electrolytes (SPEs) offer advantages such as cost-effectiveness, mechanical flexibility, and light weight; however, their practical use is hindered by limited ionic conductivity, narrow electrochemical stability window, and suboptimal cycling performance. Herein, we present a class of weakly-solvating dinitrile-based SPEs (DBSPEs) composed of a poly(2-(2-(2-methoxyethoxy)ethoxy)ethyl acrylate) network coupled with structurally modulated dinitrile solvents. Through rationale molecular engineering, the synergistic combination of short ethylene oxide side chains and weakly coordinating dinitrile solvents enables weak hybrid solvation of lithium ions, thereby facilitating rapid ion migration and uniform lithium deposition. The optimized DBSPE-2 exhibits a high ionic conductivity ($\sim$2.2 $\times$ 10^{-3} S cm^{-1}) and an extremely wide electrochemical window ($\sim$5.7 V). Notably, the Li||DBSPE-2||Li symmetric cell yields stable lithium plating/stripping over 6900 h at 0.1 mA cm^{-2} under ambient conditions (26 °C). When paired with LiFePO$_4$ in a full cell, the LMBs deliver a superior fast-charging capability, realizing 80.78% capacity retention after 1500 cycles at 2.0 C rate. This work provides fundamental insights into the solvation structure and accordingly realizes long-lasting LMBs with weak solvents.

Introduction

The rapid growth of electric vehicles urgently demands high-performance lithium-ion batteries that overcome the low-capacity dilemma of graphite electrode.[1,2] Lithium metal is seen as the most promising negative electrode candidate due to its ultra-high theoretical specific capacity ($\sim$3860 mAh g^{-1}).[3] However, the inherent incompatibility between flammable liquid electrolytes and reactive lithium surfaces persists as a critical safety barrier for practical lithium metal batteries (LMBs).[4] Solid-state polymer electrolytes

(SPEs) are recognized for their safety, cost-effectiveness and processability; however, their commercial viability is compromised by inadequate ionic conductivity, insufficient electrochemical stability, and suboptimal cycling performance.[5,6] For the extensively studied polyethylene oxide (PEO)-based SPEs, the slow movement of semi-crystalline PEO chains and strong Li$^+$–O coordinative interactions result in a low ionic conductivity (10^{-6}$\sim$10^{-7} S cm^{-1}), low lithium ions migration efficiency, and a narrow redox window ($\sim$3.8 V).[7]

The strategic incorporation of solvents into polymer matrices has emerged as an effective approach to engineer gel-type SPEs with enhanced safety and ion transport kinetics.[8,9] For example, high-polarity strong solvents, such as ethylene carbonate (EC) and 1,2-dimethoxyethane (DME), have been extensively employed to develop strongly-solvating SPEs.[10–12] In such systems, mobile solvent molecules predominantly govern the ion dissociation and transport processes.[13] Recent advances highlight succinonitrile (SN) as a unique strong solvent, leveraging its high dielectric constant to establish continuous Li$^+$ conduction pathways within polymer matrices.[14–16] However, strong solvents induce poor interface stability, high ion desolvation energy barriers, and serious polarization loss. These issues are primarily attributed to the excessively strong interaction between the solvents and ions, which excludes anions from the solvation sheath of Li$^+$ ions and fails to construct a stable solid electrolyte interface (SEI) layer.[17–19]

In sight of these limitations, weak solvents are considered as a potential alternative to conventional solvents, due to their moderate ionic desolvation energy, abundant Li$^+$ ions solvated structures and insignificant polarization losses. These features enable widespread applications of weak solvents in

[*] C. Luo, C. Ning, X. Huang, P. Zhang, L. Yang, S. Wang, J. Wang, Prof. Y. Wang, Prof. Z.-H. Guo, Prof. K. Yue
State Key Lab of Luminescent Materials and Devices, Guangdong Provincial Key Laboratory of Functional and Intelligent Hybrid Materials and Devices, Guangdong Basic Research Center of Excellence for Energy and Information Polymer Materials, South China Advanced Institute for Soft Matter Science and Technology, School of Emergent Soft Matter, South China University of Technology, Guangzhou 510640, China
E-mail: kanyue@scut.edu.cn

Prof. K. Wan, Prof. Z. Liang
Guangdong Provincial Key Laboratory of Fuel Cell Technology, School of Chemistry and Chemical Engineering, South China University of Technology, Guangzhou 510641, China
E-mail: zliang@scut.edu.cn

Prof. K. Yue
Beijing National Laboratory for Molecular Sciences, No. 2 Zhongguan Village North 1 St, Beijing 100190, China

📖 Additional supporting information can be found online in the Supporting Information section

wide-temperature-range and fast-charging LMBs.[18,20,21] The integration of weak solvents into a polymer matrix promises the development of weakly-solvating SPEs with optimized Li$^+$ coordination environments and enhanced interfacial stability.[22] For example, Huang et al. proposed that weak fluorinated solvents could facilitate the formation of moderate solvation structures around Li$^+$ ions, enabling high-voltage LMBs to operate stably at -40 °C for over 125 cycles with 87.9% capacity retention.[23] Despite these advances, the full potential of weak-solvent-engineered SPEs remains underexplored, especially concerning their compatibility with high-rate cycling and extended lifespan requirements in practical LMB applications.

In this study, we present a molecular engineering strategy to tailor dinitrile-based weakly-solvating SPEs for high-performance LMBs at room temperature. Through systematic variation of the aliphatic chain length of dinitriles, we developed one class of dinitrile-based SPEs (DBSPEs) featuring synergistic effects between rapid side-chain PEO dynamics and weak ionic coordination facilitated by –C≡N groups.[24,25] Notably, the optimized DBSPE-2 exhibits a high ionic conductivity (~2.2 × 10^{-3} S cm^{-1}), a decent Li$^+$ ion transference number ($t_{Li+} = 0.52$), and an extremely wide electrochemical window (~5.7 V). Under ambient conditions (26 °C), DBSPE-2 enables stable lithium plating/stripping for over 6900 h at 0.1 mA cm^{-2} in Li∥DBSPE-2∥Li symmetric cells, and achieves superior fast-charging performance in full cells with LiFePO$_4$ (LFP) for over 1500 cycles at 2.0 C with 80.78% capacity retention. Our DBSPEs hold potentials for achieving high-performance fast-charging LMBs operating at room temperature.

Results and Discussions

The design principles for weakly-solvating SPEs are schematically shown in Figure 1a. Specifically, weak solvents exhibit moderate coordination strength with Li$^+$ ions. The resulting hybrid solvation sheath, composed of polymer segments, anions, and solvent molecules, fosters generation of multi-constituent conductive SEI with balanced mechanical-chemical properties. Such an anion-incorporated interfacial architecture effectively homogenizes lithium-ion flux and suppresses space-charge accumulation, enabling self-regulated lithium deposition morphology (Figure 1b).[26] In contrast, strong solvents have been widely used in preparing SPEs owing to their excellent salt solubility, aiming to improve the ionic conductivity and Li$^+$ transference number (t_{Li+}). However, the aggressive solvation created by strong solvents can lead to high ion mobility barriers, sluggish desolvation kinetics, and a non-uniform Li$^+$ ions flux. Solvent-driven SEI layers also leads to irregular lithium deposition, which eventually evolves into unfavorable dendrites.[27]

To mitigate the over-solvation issue associated with the widely explored strong solvent SN, we employed a chain-extension molecular engineering strategy to develop weakly-solvating dinitrile solvents. Specifically, by systematically elongating the aliphatic carbon chain of SN, we selected four structurally modulated dinitriles, *viz.* glutarodinitrile

(GDN), adipodinitrile (ADN), heptanedinitrile (HDN), and octanedinitrile (ODN), as potential candidates. To elucidate the design principle, we first used density functional theory (DFT) calculations to probe the electrostatic potential (ESP) distributions and Li$^+$ binding energies (E$_b$) of the selected solvents (Figure S1). The benchmark strong ether solvent DME exhibits a charge-focused ESP map along with a high E$_b$ (-1.82 eV) resulting from Li$^+$–O coordination (Figure 1c). In contrast, SN displays a localized negative charge distribution and an even higher E$_b$ (-2.16 eV) via Li$^+$–N≡C coordination, due to its *gauche* conformation.[28] This comparison reveals that the inherent torsional isomerism of SN may lead to excessively strong solvation, which is undesirable for SPEs.[29] Therefore, extending the aliphatic chain of SN represents a straightforward and effective strategy for disrupting the strongly solvated structure of the Li$^+$-SN complex. Similarly, quantum mechanical calculations of the binding energy results strongly supporting the validity of our original FF-based comparative analysis (Figure S2).

Indeed, as the number of methylene spacers increases in the linear dinitriles, the –C≡N groups exhibit spatially decoupled electron distributions, weakening Li$^+$ coordination strength. Notably, ADN emerges as the optimal candidate with the weakest E$_b$ (-1.20 eV), signaling its potential for replacing conventional strong solvents (Figure S1). These DFT findings were corroborated by ^{7}Li-NMR spectroscopy. The strong Li$^+$–DME coordination induces a significant ^{7}Li chemical shift from 1.7 to 1.733 ppm (Figure 1d).[13] Similarly, the strong Li$^+$–N solvation between SN and Li$^+$ results in a shift from 1.7 to 1.664 ppm.[17,30] However, the small shifts observed in Li$^+$–GDN (1.7 to 1.675 ppm), Li$^+$–ADN (1.7 to 1.676 ppm), Li$^+$–HDN (1.7 to 1.677 ppm), and Li$^+$–ODN (1.7 to 1.695 ppm) suggest that the selected chain-extended dinitriles indeed exert weak solvation on Li$^+$ ions (Figure S3). In particular, ODN exhibits a minimal chemical shift in the ^{7}Li-NMR spectrum compared to GDN, ADN, and HDN, indicating its low polarity and excessively poor solvation capability in the presence of DMSO-d_6 as the solvent.

The frontier molecular orbital energetics of solvents and their Li$^+$ complexes, as calculated by DFT, provide critical insights into electrochemical stability (Figure 1e). The highest occupied molecular orbital (HOMO) and lowest unoccupied molecular orbital (LUMO) energy levels directly correlate with a solvent's oxidative resistance and reductive activity, respectively.[10] For safe LMBs, solvents with low LUMO energy levels are crucial for facilitating the rapid reductive formation of a stable SEI layer on the lithium metal electrode.[31] The HOMO/LUMO energies of the five nitrile molecules (SN, GDN, ADN, HDN, and ODN) are calculated as -12.68/4.32, -12.69/4.25, -12.54/4.75, -12.39/4.79, and -12.29/5.01 eV, respectively, compared to -11.13/6.49 eV for DME. This comparison highlights the superior electron-accepting capability of dinitriles at the anode, promoting accelerated SEI formation and, consequently, dendrite suppression.[31]

Upon Li$^+$ coordination, all Li$^+$–dinitrile complexes exhibit a reduction in LUMO energy levels. Notably, the Li$^+$–SN complex shows a drastic bandgap narrowing, leading to excessive reducibility and oxidative vulnerability. This high
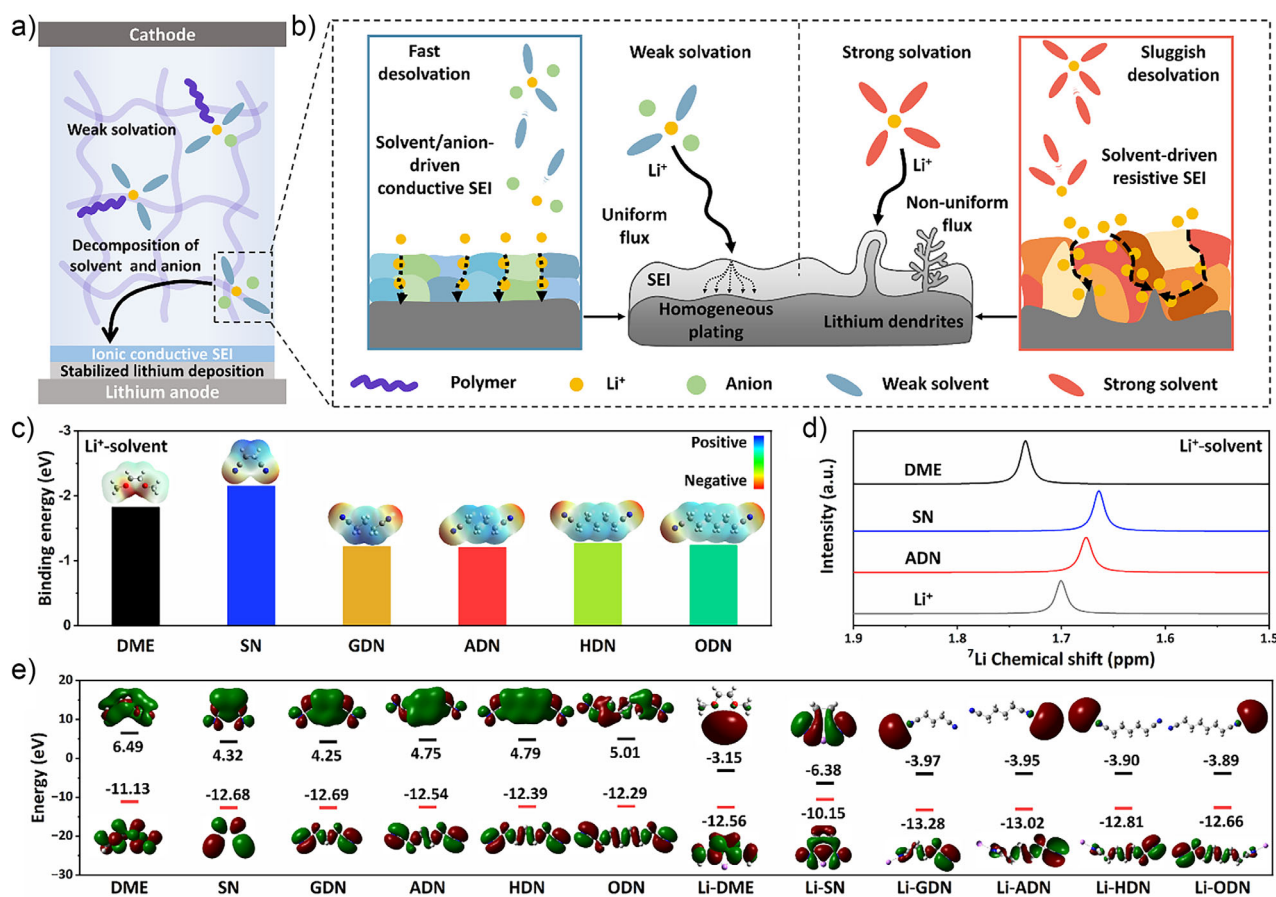
Figure 1. a) Schematic illustration of a weakly-solvating SPE. b) Schematic comparison of the solvation behaviors of weak and strong solvents. The weak solvent facilitates the co-participation of other components in ion solvation sheath and thus the formation of an ionic conductive SEI. The weakened binding promotes fast desolvation of Li$^+$ ions to form uniform flux for homogeneous plating. In contrast, strong solvents tightly coordinate with Li$^+$ ions, induce sluggish desolvation and decompose to form solvent-driven SEI layer. The thick and resistive SEI is detrimental to inhibition of lithium dendrites growth. c) Binding energy of different solvent molecules with Li$^+$ and solvent-specific ESP distributions. d) ^{7}Li-NMR spectra of different solvent molecules with Li$^+$. e) Differences in HOMO/LUMO energies of different solvents and complexes with Li$^+$. Spheres color code: Li (purple), C (gray), H (white), O (red), N (blue).

excitability of SN might lead to undesirable side reactions and interfacial instability, ultimately causing rapid solvent depletion.[10,32] In contrast, the chain-extended dinitriles possess a moderate LUMO depression for controlled SEI generation, while preserving large HOMO-LUMO gaps to ensure chemical robustness. Therefore, dinitriles with extended aliphatic carbon chains are promising weak solvent candidates for long-lasting LMBs.

Based on the solvent design rationale, five DBSPEs are developed by infiltrating SN, GDN, ADN, HDN, or ODN into a poly(2-(2-(2-methoxyethoxy)ethoxy)ethyl acrylate) (PMEEA) network, which are designated as DBSPE-0 to DBSPE-4, respectively. Note that the PMEEA network was selected as the polymer matrix featured with a moderate PEO side-chain length and balanced solvent-polymer coordination with Li$^+$ ions, which are desirable for the synergistic cooperation of solvent and polymer for Li$^+$ transport.[24,33–35] The SN-based DBSPE-0, previously reported in our earlier work,[24] is used as a benchmark for comparison. The DBSPEs are prepared in situ at 80 °C within an encapsulated battery via the thermal-induced

polymerization from a precursor solution. The homogeneous solution contains lithium bis(trifluoromethanesulfonyl)imide (LiTFSI), the monomer, the dinitrile, a crosslinker, and 2,2′-azobis(2-methylpropionitrile) (AIBN) as the thermal initiator. As a control, a DME-incorporated PMEEA SPE (an ether-based SPEs, or EBSPE) is fabricated in the same way. The in situ polymerization process yields optically transparent, freestanding DBSPE membranes (Figure S4) that conformally coat the lithium electrodes. The representative thickness value of the as-prepared SPEs is about 130 μm, as revealed by cross-sectional SEM imaging (Figure S5). This conformal coating significantly improves the air stability by preventing metallic lithium oxidation (Figure S6a,b). The mechanical properties of the DBSPEs were also investigated by uniaxial tensile tests. As shown in Figure S7a,b, all the DBSPEs possess high Young's modulus (>1.0 MPa), which is desirable for the suppression of dendrites formation.[36] And thermogravimetric analysis confirms the robust thermal stability of the as-prepared DBSPEs, evidenced by a 5% weight loss temperature exceeding 100 °C (Figure S8). Similarly, the differential scanning calorimetry (DSC) analysis
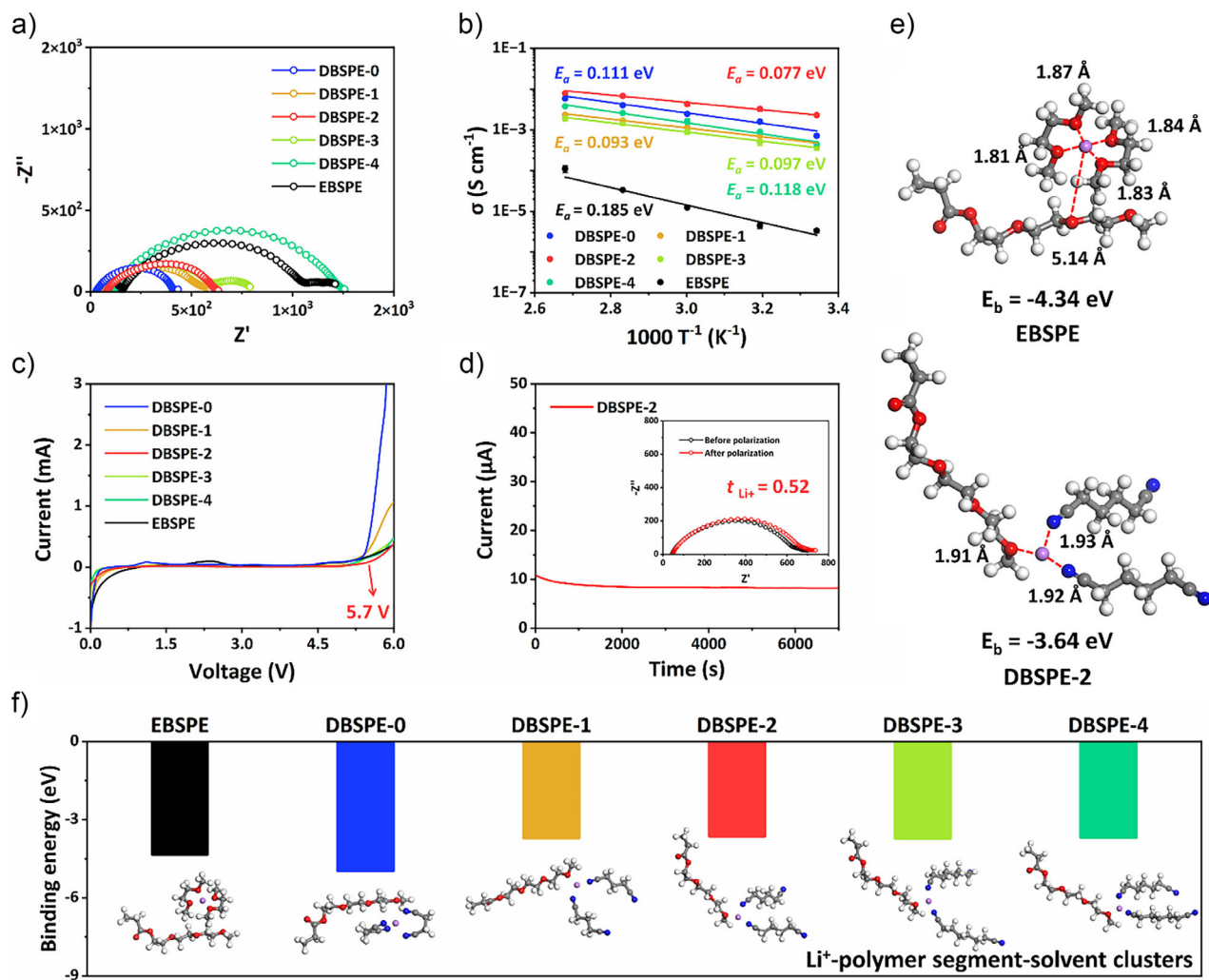
Figure 2. Electrochemical characterization of DBSPEs. a) Interfacial impedance of DBSPEs measured in Li‖Li symmetric cells. b) Arrhenius plots of the DBSPEs based on measurement of ionic conductivity versus temperature. c) LSV curves of the DBSPEs. d) t_{Li+} value of DBSPE-2 measured by chronoamperometry, with corresponding impedance spectra before and after polarization. e) Optimal structures of the Li$^+$ ions in the polymer segment with different solvents. f) Binding energies and simplified models of optimized structures for different clusters.

confirms the thermally invariant behavior of DBSPEs over −50.0 °C to 70.0 °C (Figure S9), which is often observed in highly crosslinked polymer networks.[37–39]

Attenuated total reflectance Fourier transform infrared (ATR FT-IR) spectroscopy was used to monitor the in situ polymerization process. The disappearance of the C=C bond absorption peak (1636 cm^{-1}) confirms successful polymerization (Figure S10a). The absence of monomer residue in the as-prepared SPE samples is further confirmed by ^{1}H NMR analysis (Figure S11). The presence of a sharp absorption peak of −C≡N groups at 2550 cm^{-1} indicates the presence of dinitrile, while the shoulder peaks at 2274 cm^{-1} are attributed to Li$^+$–coordinated cyano groups.[40] Shifts in multiple absorption peaks at 1680–1860 and 1185 cm^{-1} may reflect Li$^+$–O interactions.[41] Notably, the absorption peaks of S−N−S and O=S=O in TFSI$^-$ anions are observed at near 1055 and 1351 cm^{-1}, respectively, suggesting the participation of free anions in constructing the solvation sheath of the Li$^+$ ions (Figure S10b).[25]

Small-angle X-ray scattering (SAXS) profiles show featureless scattering without distinct peaks (Figure S12), while wide-angle X-ray diffraction (WAXD) patterns display only a single diffraction halo. These results confirm the homogeneous amorphous structure of the DBSPEs (Figure S13). The tailored weak solvation environment in DBSPEs promotes the miscibility among the different components. This amorphous structure of DBSPEs likely enables a uniform ion flux distribution and low tortuosity transport pathway, which can suppress the dendrite formation.[42]

We further evaluated the electrochemical properties of the weakly solvating DBSPEs. Electrochemical impedance spectra (EIS) reveal that the interfacial resistance increases with the dinitrile chain length, from 433 Ω for DBSPE-0 to 1139 Ω for DBSPE-4 (Figure 2a). This trend can be attributed to the reduced effective cyano group density. In comparison, EBSPE exhibits a much higher intrinsic and interfacial impedance. The Arrhenius plots (Figure 2b) show the temperature-dependent ionic conductivity of DBSPEs
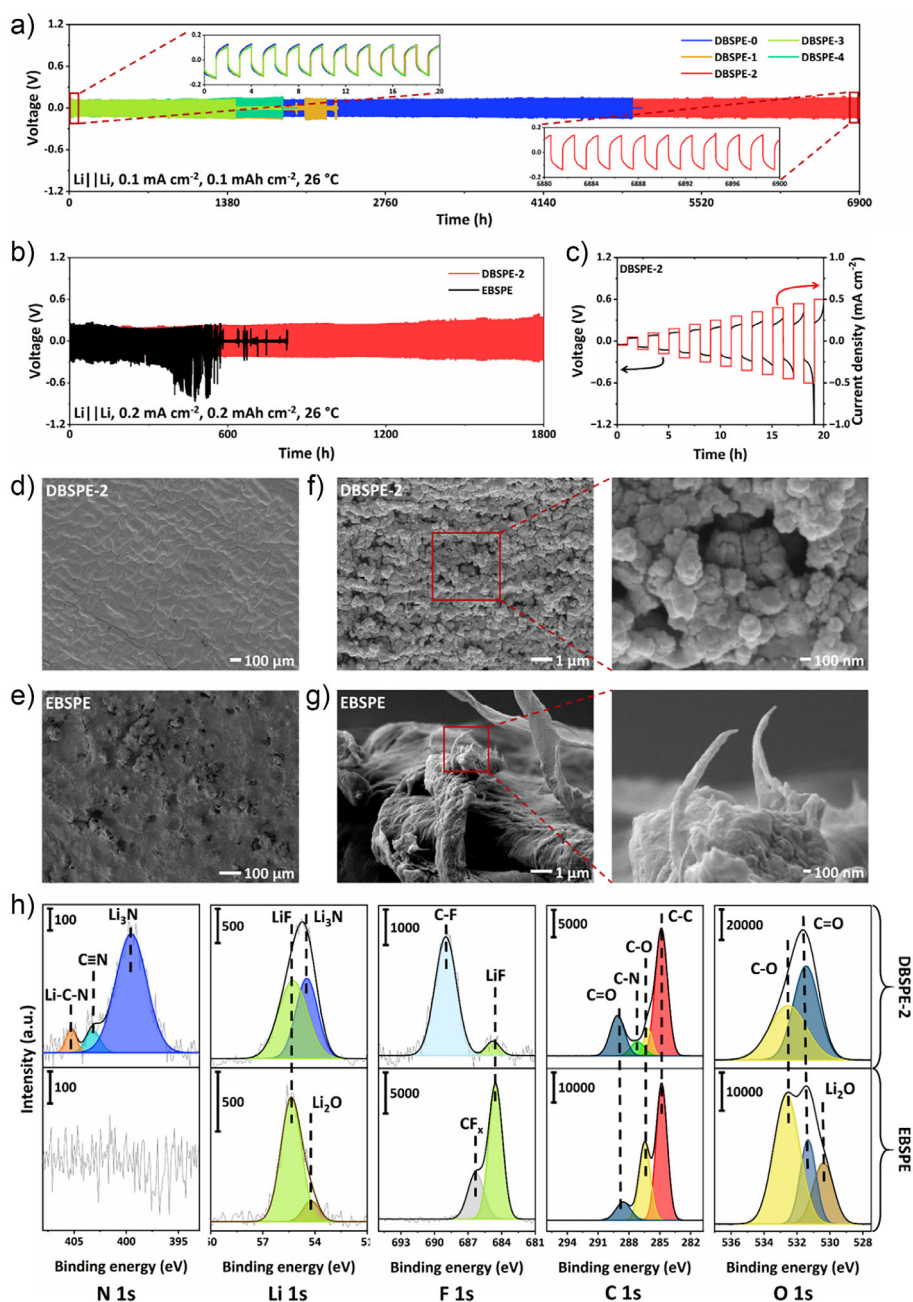
Figure 3. Electrochemical performance and structural evolution of DBSPEs and EBSPE in Li||Li symmetric cells. a) Galvanostatic cycling performance of DBSPEs in Li||Li symmetric cells at 0.1 mA cm^{-2}. b) Galvanostatic cycling performance of DBSPE-2 and EBSPE in Li||Li symmetric cells at 0.2 mA cm^{-2}. c) Critical current density of DBSPE-2. SEM characterization revealing surface morphology of d) DBSPE-2 and e) EBSPE after cycling in Figure 3b. Top-view SEM images of lithium deposition morphology in Li||Li symmetric cells made of (f) DBSPE-2 and (g) EBSPE. h) XPS spectra of the Li electrode in DBSPE-2 and EBSPE cells, including N 1s, Li 1s, F 1s, C 1s, and O 1s (from left to right).

(corresponding EIS shown in Figure S14a-f). Notably, DBSPE-2 exhibits the highest room-temperature ionic conductivity ($\sim$2.2 $\times$ 10^{-3} S cm^{-1}) among the DBSPEs, which might stem from the odd-even effect of aliphatic nitriles.[43,44] The calculated activation energy (E_a) for the Li$^+$ ion transport in DBSPE-2 is low (0.077 eV), which is consistent with the lowest calculated E$_b$ (-1.20 eV) for ADN (Figure 1c). This low energy barrier facilitates the rapid ion desolvation kinetics, thereby promoting multicomponent participation in the ion transport.[26] In contrast, the low conductivity and high

E_a of EBSPE suggest that the Li$^+$–DME complex suffers from a low ion transport kinetics through the PMEEA network.[20]

To evaluate the voltage tolerance of DBSPEs, we performed linear sweep voltammetry (LSV) to determine the electrochemical window. Due to the high electron affinity and stability of cyano groups, DBSPE-2 exhibits a wide potential window up to 5.7 V (Figures 2c and S15), surpassing the other SPEs. The well-defined redox peaks in the cyclic voltammetry (CV) curves demonstrate the reliable reversibility of Li$^+$ in DBSPEs (Figure S16).[45] To assess the cation transport

Angew. Chem. Int. Ed. **2025**, 64, e202507051 (5 of 11)

© 2025 Wiley-VCH GmbH

selectivity, we measured the Li^+ transference number (t_{Li+}) using the Bruce-Vincent method. Figure 2d presents the time-dependent current polarization curves for DBSPE-2 measured by the chronoamperometry, with the EIS being collected before and after polarization (Figure S17). Among the SPEs, DBSPE-2 exhibits a decent t_{Li+} value of 0.52, which is lower than that of DBSPE-0. This is probably due to the special fast lithium conduction mechanism of the plastic crystalline phase associated with SN (Figure S18).[14]

The superior electrochemical performance of DBSPE-2 is primarily attributed to the synergistic weak solvation arising from the interplay between ADN and the PMEEA network. Such a design promotes a diversified hybrid solvation environment to mitigate the undesirable concentrated distribution of ions; in comparison, the ion transport is primarily driven by the solvent polarization for the strongly solvating SPEs.[23] We performed DFT calculations to validate the proposed weakened hybrid solvation in DBSPE-2. Figure 2e illustrates the optimized cluster structures of Li^+ ions within a polymer segment in the presence of different solvents. In this simplified model, one single Li^+ ion exhibits distinct solvation preferences in complexes with one polymer segment and two solvent molecules. In EBSPE, the strongly solvating DME dominates the solvation shell of the Li^+ ion, effectively excluding the polymer segment to a distance of 5.14 Å, with an E_b of -4.34 eV. Conversely, the weakly solvating ADN in DBSPE-2 facilitates co-solvation of the Li^+ ion with the polymer segment, resulting in a lower E_b of -3.63 eV. Figure 2f summarizes the optimized structural binding energies of various solvent/polymer chain segment/Li^+ clusters based on the simulation models. It is important to note that the formation of SN-like *gauche* isomers from the chain-extended dinitriles is unfavorable due to the spatial site-barrier effect.[24] This mechanistic understanding reinforces our molecular design of DBSPEs with weakened hybrid solvation. To further describe the representative solvation models, molecular dynamics (MD) simulations were employed to analyze the radial distribution functions (RDFs) and associated lithium coordination numbers ($N(r)$) of DBSPE-2 and EBSPE (Figure S19). The results show that the weakened hybrid solvation of DBSPE causes similar $N(r)$ for the polymer-Li^+ (Li^+-O) and ADN-Li^+ (Li^+-O), whereas the O atoms in the polymer in EBSPE hardly coordinate with Li^+, demonstrating the over-solvation of DME.

We further evaluated the lithium reversibility using Li‖Li symmetric cells. Initial screening shows that all the DBSPEs exhibit stable galvanostatic cycling performance for up to 1400 h at 0.1 mA cm^{-2} (Figure S20). Remarkably, the Li‖DBSPE-2‖Li cell stably runs over 6900 h and maintains a highly stable polarization potential of ~100 mV (Figure 3a), suggesting uniform and stable ion migration. The virtually unchanged polarization potentials in the initial and final 20-h time-voltage curves (Figure 3a, inset) highlight the superior interfacial compatibility and cyclability of DBSPE-2. Under identical conditions, DBSPE-2 significantly outperforms the other DBSPE counterparts in the cycling stability. In addition, the Li‖DBSPE-2‖Li cell exhibits stable Li plating/stripping over 1800 h at 0.2 mA cm^{-1}, without a significant change

in the polarization voltage (Figure 3b). In contrast, the EBSPE shows an increased polarization voltage after 300 h, suggesting undesired side reactions occur at the interface. Meanwhile, DBSPE-2 achieves a critical current density (CCD) of 0.45 mA cm^{-2} in Li‖Li symmetric cells (Figure 3c), indicating its potential for high current-density applications. As shown in Figure S21, a rate cycling stability test was performed on DBSPE-2 between 0.1 and 0.3 mA cm^{-2} in a Li‖Li symmetric cell, revealing that the DBSPE-2 can adapt to the fast input current switching and remain stable for 100 h. The absence of voltage surges or dips during cycling indicates the suppressed dendrite formation.[46]

Postmortem scanning electron microscope (SEM) analysis of cycled cells (from Figure 3b) unveiled mechanistic insights into the morphological change of the electrolyte. After 1800-h cycling, the DBSPE-2 maintains an intimate electrode-electrolyte contact with a uniform surface morphology (Figure 3d).

In contrast, fragmented holes appear on the EBSPE surface, likely caused by uncontrolled lithium dendrite growth (Figure 3e). The lithium electrode surface in contact with DBSPE-2 shows abundant, homogeneous granular lithium deposits of even size (Figure 3f), which results from the regulated ion flux through weakened solvation channels (Figure 1). In comparison, the EBSPE exhibits rampant dendritic growth with penetrative protrusions (Figure 3g), directly linking strong solvent dominance to catastrophic interfacial failure.

The SEI compositional difference between the lithium electrode and electrolyte is investigated by the complementary X-ray photoelectron spectroscopy (XPS) to visualize the distinct evolutionary pathways of the interface structure. The wide-scan spectrum (Figure S22) shows five main peaks at 284.8 eV (C 1s), 531.8 eV (O 1s), 668.8 eV (F 1s), 398.8 eV (N 1s), and 54.8 eV (Li 1s) for the SEI layer in DBSPE-2, while the spectrum of the EBSPE shows negligible nitrogen signals. High-resolution N 1s spectra (Figure 3h) unveil Li_3N (399.6 eV), C≡N (403.2 eV), and cyano-derived Li—C—N (405.3 eV) species exclusively in DBSPE-2.

Deconvolution of the Li 1s spectrum confirms the formation of highly conductive Li_3N (54.9 eV) and electrochemically inert LiF (55.7 eV) in the SEI layer of DBSPE-2, resulting from the decomposition of ADN and TFSI$^-$. The LiF peak in the EBSPE-based electrode likely originates from the incomplete shedding of —CF_3 groups from TFSI$^-$.[47] Meanwhile, the Li_2O peak (54.2 eV) may originate from the interfacial decomposition of DME. The F 1s spectra reveal different degrees of anion involvement in the chemical reactions of the two electrolytes. In DBSPE-2, the strong peak of C—F at 689.0 eV likely arises from the decomposition of CF_3 groups in TFSI$^-$, indicating that exposed F and N atoms in anions are deeply involved in SEI formation.[48] In contrast, the strong CF_x peak at 686.3 eV observed in EBSPE suggests that most of the F atoms on CF_3 remain undetached, as the solvation and interfacial reactions are dominated by the strong solvent DME.[47]

The C 1s spectrum of DBSPE-2 shows multiple overlapping characteristic peaks. The main peak (284.8 eV) and side peaks (286.3, 289.8 eV) are categorized as hydrocarbon
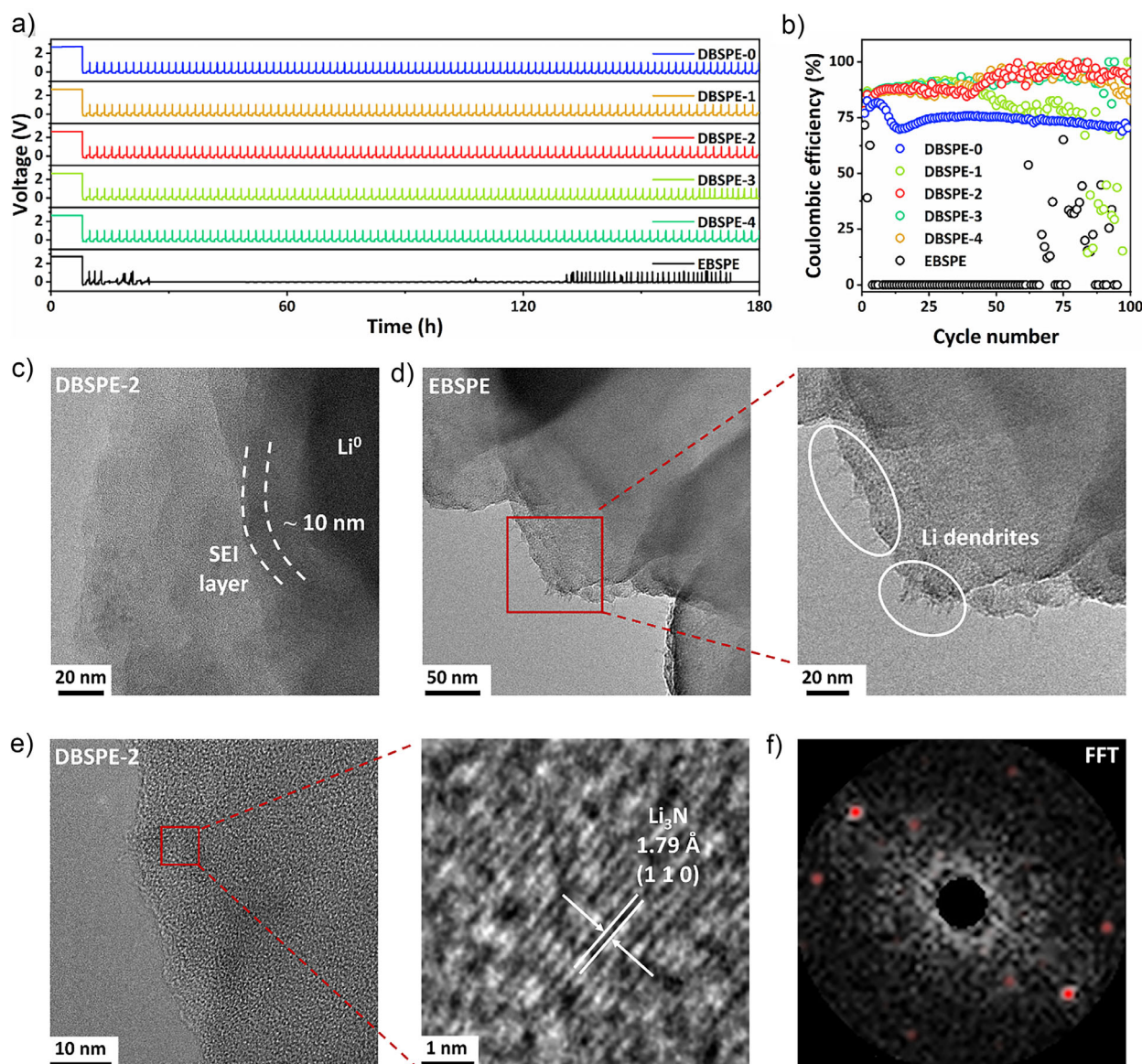
Figure 4. Lithium cycling efficiency and interphase analysis of DBSPE-2 and EBSPE in Li‖Cu asymmetric cells. a) Time-voltage profiles of different Li‖Cu asymmetric cells at 0.1 mA cm⁻². b) Coulombic efficiency for different Li‖Cu asymmetric cells. c) High-magnification TEM image of the SEI layer in a DBSPE-2 cell. d) TEM images of lithium dendrites in an EBSPE cell. e) TEM image of Li_3N lattice with local magnification. f) FFT pattern of the TEM image with detected Li_3N lattice spots marked by red dots.

species, including C—C, C—O, C=O bonds.[14] The peak at 287.5 eV likely originates from the C—N bond generated by the reductive decomposition of ADN and anions, which are not detected in EBSPE. Additionally, the O 1s spectrum of DBSPE-2 displays two major peaks associated with the carbon-oxygen bond at 532.8 eV (C—O) and 531.3 eV (C=O), respectively. The peak at 530.4 eV in EBSPE is probably related to the Li_2O, which matches the Li 1s spectra.[49]

Collectively, we believe that the exceptionally stable cycling performance of the DBSPE-2-based Li‖Li symmetric cell stems from the weak solvent ADN, which facilitates the formation of a Li_3N-rich and LiF-rich SEI layer. And both the robust conductive interphase and regular ionic kinetics enable the long-lasting and safe operation of LMBs.[27,50,51] The

stark contrast with the solvent-driven SEI failure in EBSPE underscores the weak-solvent engineering as a promising strategy for durable LMBs.

Li‖Cu asymmetric cells were assembled to determine the lithium coulombic efficiency (CE), a key indicator for analyzing lithium stripping/depositing behavior.[52,53] Complete lithium stripping/depositing on the Cu electrode was performed until reaching a cut-off voltage of 1 V, at a current density of 0.1 mA cm⁻² for 100 cycles. The time-voltage profiles reveal that DBSPEs maintain a stable potential throughout the 100 cycles (Figure 4a). In contrast, the EBSPE exhibits an erratic voltage profile and a sharp decrease in the CE. The average CE values are 74.16% for DBSPE-0, 90.81% for DBSPE-1, 91.44% for DBSPE-2, 78.42% for DBSPE-3, 90.66% for DBSPE-4, and 9.11% for EBSPE (Figure 4b).
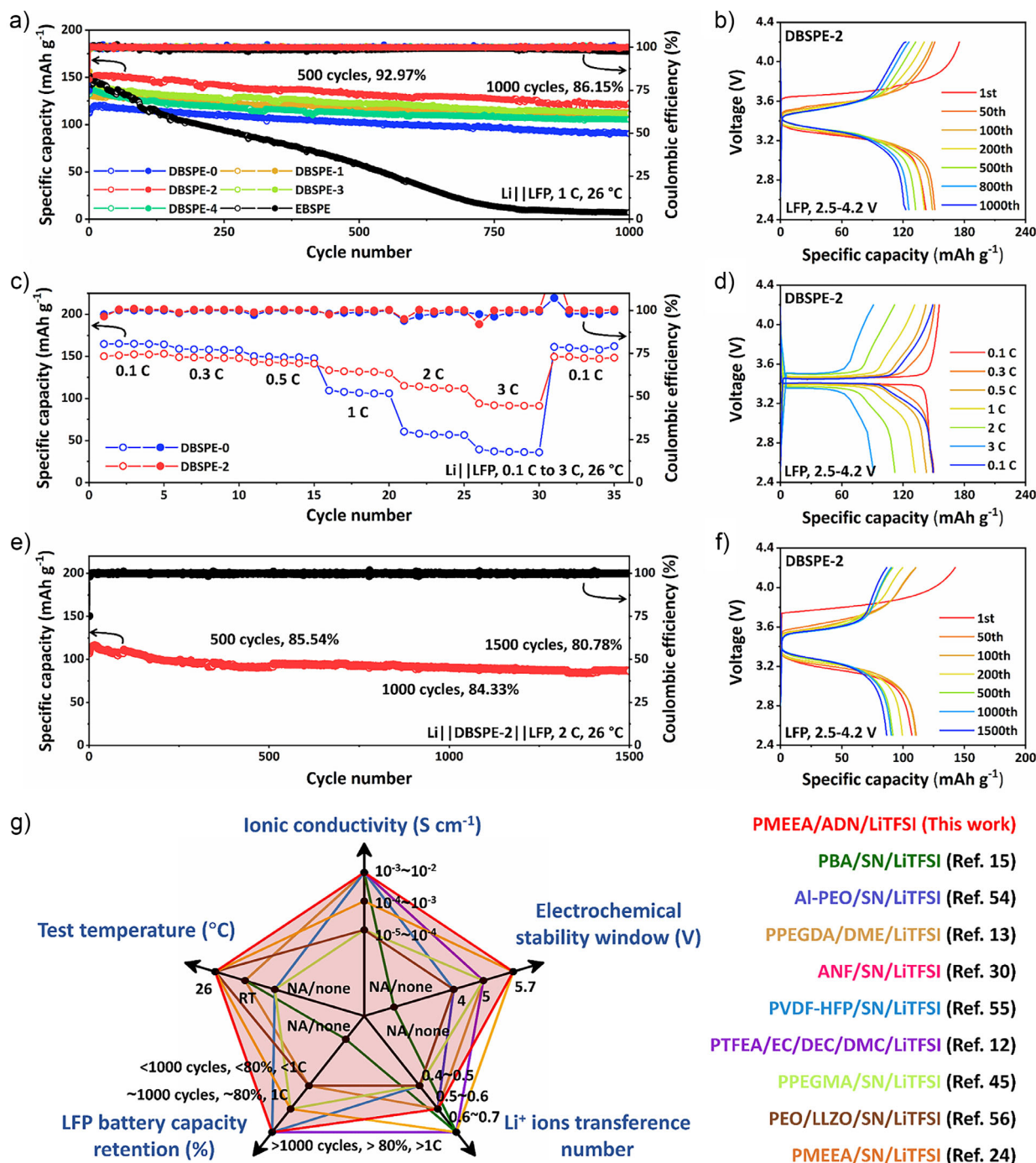
Figure 5. Cycling performance of DBSPEs-based full cells. a) Long-term cycling performance of LFP LMBs based on DBSPEs and EBSPE at 1.0 C rate and 26 °C. b) Charged/discharged curves corresponding to a Li||DBSPE-2||LFP cell over 1000 cycles. c) Rate performance comparison between a Li||DBSPE-2||LFP full cell and a Li||DBSPE-0||LFP full cell. d) Specific capacity-voltage curves with different rates. e) Long-term cycling performance of LFP LMBs based on DBSPE-2 at 2.0 C rate and 26 °C. f) Charged/discharged curves corresponding to a Li||DBSPE-2||LFP cell over 1500 cycles. g) A rough comparison between the cells based on DBSPE-2 reported in this work and previously reported representative gel-type electrolytes, in terms of ionic conductivity, electrochemical stability window, Li$^+$ ions transference number, test temperature, and LFP battery capacity retention.[12,13,15,24,30,45,54–56]

Moreover, the capacity-voltage curves of the DBSPE-2 show repeatable lithium recycling (Figure S23).

After 100 cycles, the tests were terminated when lithium was deposited on the Cu electrode, and the cells were disassembled for the SEM characterization. Top-view SEM images reveal that the DBSPE-2 facilitates uniform and continuous granular lithium deposition (Figure S24), indicating an unobstructed ion flux. Conversely, the EBSPE exhibits unevenly distributed lithium deposits with a lumpy morphology (Figure S25). These results indicate that the

DBSPEs offer stable and facile lithium transport, which substantially enhance the battery's durability and lifespan.

Given the different cycling performance in Li||Cu asymmetric cells, we conducted cross-sectional transmission electron microscope (TEM) analysis of the cycled lithium electrodes to elucidate the SEI evolution. The DBSPE-2 yields a well-defined compact SEI layer (~10 nm) with sharp interface delineation (Figure 4c), which is indicative of spatially uniform lithium deposition. In contrast, the edges of the lithium deposited in the EBSPE cells show an irregular burr-like shape, indicating the emergence of lithium dendrite (Figure 4d). Notably, local magnified images of the SEI layer derived from the DBSPE-2 reveal the presence of the Li_3N lattice (Figure 4e), as evidenced by the fast Fourier transform (FFT) pattern with Li_3N lattice spots (red markers in Figure 4f). This result confirms that the weak solvents and anions are effectively involved in constructing the N-rich SEI layer through interfacial reactions.[27,49]

Li||LFP full cells were assembled to evaluate the performance of DBSPEs in LMBs. The mass loading of active cathodes is fixed at approximately 1.5 mg unless otherwise specified. Due to the wide electrochemical window, DBSPEs enable the charge/discharge test in LFP-based LMBs within the 2.5–4.2 V range. As shown in Figure 5a, DBSPEs exhibit a decent initial discharge specific capacity, high first-cycle CE, and superior capacity retention after 1000 cycles. Specifically, the Li||DBSPE-2||LFP full cell achieves an initial discharge specific capacity of 142.3 mAh g^{-1} with the first-cycle CE of 81.25% at 1.0 C rate. After 500 cycles, the capacity slightly decays to 132.3 mAh g^{-1}, which corresponds to a high-capacity retention of 91.85%. After 1000 cycles, the discharge specific capacity is 122.6 mAh g^{-1}, with a retention of 86.15%. In contrast, the EBSPE exhibits an inferior cycling performance. Its initial discharge specific capacity is 138.5 mAh g^{-1}, which drastically decays to zero after 1000 cycles. The charge/discharge capacity-voltage curves of the DBSPE-2-based cell (Figure 5b) show minimal voltage hysteresis, suggesting negligible side reactions.

The Li||DBSPE-2||LFP full cell also demonstrates superior rate capability under standard charge/discharge voltages (Figures 5c,d and S26). Specifically, the cell exhibits reversible and stable discharge specific capacity of 150.1, 149.2, 142.9, 131.7, 112.1, and 90.9 mAh g^{-1} at 0.1, 0.3, 0.5, 1.0, 2.0, and 3.0 C, respectively. Notably, upon returning the rate from 3.0 to 0.1 C, the discharge capacity recovers to 149.4 mAh g^{-1}, which is approximate to the initial one and reveals the rapid ion transport kinetics. However, the over-solvation of SN compromises the fast-charging capability of the Li||DBSPE-0||LFP full cell, consistent with previous reports.[24,45]

Figure 5e presents the fast charge/discharge performance (at 2.0 C) of LFP-based cells using DBSPE-2. The Li||DBSPE-2||LFP full cell delivers a discharge capacity of 107.2 mAh g^{-1} in the first cycle with a first-cycle CE of 75.23%. Remarkably, the capacity shows a mild decrease to 91.7 mAh g^{-1} after 500 cycles and 90.4 mAh g^{-1} after 1000 cycles, realizing the capacity retention of 85.54% and 84.33%, respectively. After 1500 cycles, the discharge specific capacity decays to 86.6 mAh g^{-1}, with a high retention of 80.78%. The stable charge/discharge capacity-voltage curves demonstrate that the weakly-solvating SPE facilitates both high capacity and fast charging (Figure 5f).

Also, the performance with a high-voltage NCM cathode was investigated. As shown in Figure S27, the NCM622 cathode was used to evaluate the performance of LMBs based on DBSPE-2. The specific capacity decreases from 144.5 to 95.9 mAh g^{-1} after 100 cycles at 0.1 C, with an initial CE of 76.59% over the voltage range of 3.0–4.25 V (Figure S28). The cycling performance and capacity-voltage curves of a Li||DBSPE-2||NCM622 cell at 0.2 C are present in Figures S29 and S30. The specific capacity of this cell decreases from 160.0 to 72.7 mAh g^{-1} after 100 cycles with a high initial CE of 92.04%, suggesting the practical applications of DBSPE-2 in LMBs with NCM cathodes.

The comprehensive properties of the DBSPE-2 electrolyte, based on molecularly tailored weakly-solvating ADN, are evaluated through a comparative analysis with the recently reported gel-type electrolytes across five key parameters: ionic conductivity, electrochemical stability window, Li$^+$ transference number, test temperature, and LFP battery capacity retention. Figure 5g and Table S1 reveal that the DBSPE-2 outperforms its counterparts in the LFP-LMBs.

Conclusion

In summary, this work establishes a molecular engineering strategy using a series of dinitrile weak solvents for the construction of high-performance SPEs with tailored weak hybrid solvation. The optimized DBSPE-2 with ADN as the weak solvent showcases a combination of high ionic conductivity (~2.2 mS cm^{-1} at 26 °C), wide electrochemical stability (~5.7 V), and improved Li$^+$ transference number (~0.52). The tailored weak solvents also promote anionic participation and derivatization of the SEI layer, supporting stable electrolyte cycling. Specifically, Li||Li symmetric cells using DBSPE-2 can sustain stable lithium plating/stripping for 6900 h at a current density of 0.1 mA cm^{-1}. Using the same electrolyte, the LFP-based LMB demonstrated high durability and fast-charging capability, with only a 19.22% capacity reduction after 1500 cycles at a 2.0 C rate under ambient conditions. This performance is primarily attributed to the weak solvent/anion-derived SEI layers containing Li_3N-rich superionic conductors. This work provides molecular-scale insights for the design of weak solvents and the development of high-performance SPEs.

Acknowledgements

Conflict of Interests

The authors declare no conflict of interest.

Data Availability Statement

The data that support the findings of this study are available from the corresponding author upon reasonable request.

Keywords: Dinitrile · Lithium metal battery · Solid-state polymer electrolyte · Weak solvation

[1] Y. S. Meng, V. Srinivasan, K. Xu, *Science* **2022**, *378*, eabq3750.

[2] S. Chen, G. Wu, H. Jiang, J. Wang, T. Chen, C. Han, W. Wang, R. Yang, J. Zhao, Z. Tang, X. Gong, C. Li, M. Zhu, K. Zhang, Y. Xu, Y. Wang, Z. Hu, P. Chen, B. Wang, K. Zhang, Y. Xia, H. Peng, Y. Gao, *Nature* **2025**, *638*, 676–683.

[3] Q. Xu, T. Li, Z. Ju, G. Chen, D. Ye, G. I. N. Waterhouse, Y. Lu, X. Lai, G. Zhou, L. Guo, K. Yan, X. Tao, H. Li, Y. Qiu, *Nature* **2025**, *637*, 339–346.

[4] D. Lu, R. Li, M. M. Rahman, P. Yu, L. Lv, S. Yang, Y. Huang, C. Sun, S. Zhang, H. Zhang, J. Zhang, X. Xiao, T. Deng, L. Fan, L. Chen, J. Wang, E. Hu, C. Wang, X. Fan, *Nature* **2024**, *627*, 101–107.

[5] Y. Liu, Z. Jin, Z. Liu, H. Xu, F. Sun, X. Q. Zhang, T. Chen, C. Wang, *Angew. Chem. Int. Ed.* **2024**, *63*, e202405802.

[6] G. Ye, L. Zhu, Y. Ma, M. He, C. Zheng, K. Shen, X. Hong, Z. Xiao, Y. Jia, P. Gao, Q. Pang, *J. Am. Chem. Soc.* **2024**, *146*, 27668–27678.

[7] Y. Wang, Z. Wu, F. M. Azad, Y. Zhu, L. Wang, C. J. Hawker, A. K. Whittaker, M. Forsyth, C. Zhang, *Nat. Rev. Mater.* **2023**, *9*, 119–133.

[8] X. Cheng, J. Pan, Y. Zhao, M. Liao, H. Peng, *Adv. Energy Mater.* **2017**, *8*, 1702184.

[9] X. Zhou, Y. Zhou, L. Yu, L. Qi, K.-S. Oh, P. Hu, S.-Y. Lee, C. Chen, *Chem. Soc. Rev.* **2024**, *53*, 5291–5337.

[10] X. Liu, J. Zhang, X. Yun, J. Li, H. Yu, L. Peng, Z. Xi, R. Wang, L. Yang, W. Xie, J. Chen, Q. Zhao, *Angew. Chem. Int. Ed.* **2024**, *63*, e202406596.

[11] X. Deng, J. Chen, X. Jia, X. Da, Y. Zhao, Y. Gao, Y. Gao, X. Kong, S. Ding, G. Gao, *Angew. Chem. Int. Ed.* **2024**, *63*, e202410818.

[12] X. Miao, J. Hong, S. Huang, C. Huang, Y. Liu, M. Liu, Q. Zhang, H. Jin, *Adv. Funct. Mater.* **2024**, *35*, 2411751.

[13] M. Zhou, W. Chen, H. Yang, Y. Hu, T. Lei, D. Chen, S. Wang, Y. Zhang, J. Xiong, *Adv. Energy Mater.* **2024**, *15*, 2403082.

[14] M. J. Lee, J. Han, K. Lee, Y. J. Lee, B. G. Kim, K.-N. Jung, B. J. Kim, S. W. Lee, *Nature* **2022**, *601*, 217–222.

[15] J. Han, M. J. Lee, K. Lee, Y. J. Lee, S. H. Kwon, J. H. Min, E. Lee, W. Lee, S. W. Lee, B. J. Kim, *Adv. Mater.* **2022**, *35*, 2205194.

[16] J. Han, M. J. Lee, J. H. Min, K. H. Kim, K. Lee, S. H. Kwon, J. Park, K. Ryu, H. Seong, H. Kang, E. Lee, S. W. Lee, B. J. Kim, *Adv. Funct. Mater.* **2024**, *34*, 2310801.

[17] L. Zhao, A. Xu, Y. Cheng, H. Xu, L. Xu, L. Mai, *Angew. Chem. Int. Ed.* **2024**, *63*, e202411224.

[18] Z. Wang, B. Zhang, *Energy Mater. Dev.* **2023**, *1*, 9370003.

[19] Z. Chang, H. Yang, Y. Qiao, X. Zhu, P. He, H. Zhou, *Adv. Mater.* **2022**, *34*, 2201339.

[20] T. Ma, Y. Ni, Q. Wang, W. Zhang, S. Jin, S. Zheng, X. Yang, Y. Hou, Z. Tao, J. Chen, *Angew. Chem. Int. Ed.* **2022**, *61*, e202207927.

[21] X. Zhu, J. Chen, G. Liu, Y. Mo, Y. Xie, K. Zhou, Y. Wang, X. Dong, *Angew. Chem. Int. Ed.* **2024**, *64*, e202412859.

[22] X. Chen, C. Qin, F. Chu, F. Li, J. Liu, F. Wu, *Energy Environ. Sci.* **2025**, *18*, 910–922.

[23] Y. Wei, H. Wang, X. Lin, T. Wang, Y. Cui, Y. Huang, J. Yang, T.-H. Liu, Y. Ren, X. Fan, H. Xu, Y. Huang, *Energy Environ. Sci.* **2025**, *18*, 786–798.

[24] C. Luo, W. Ou, Y. Chen, P. Zhang, A. Li, S. Wang, M. Fu, Z.-H. Guo, K. Yue, *ACS Appl. Energy Mater.* **2024**, *8*, 306–318.

[25] C. Luo, Y. Chen, Z. Huang, M. Fu, W. Ou, T. Huang, K. Yue, *Adv. Funct. Mater.* **2023**, *33*, 2304486.

[26] H. Zhang, Z. Zeng, F. Ma, Q. Wu, X. Wang, S. Cheng, J. Xie, *Angew. Chem. Int. Ed.* **2023**, *62*, e202300771.

[27] M. S. Kim, Z. Zhang, J. Wang, S. T. Oyakhire, S. C. Kim, Z. Yu, Y. Chen, D. T. Boyle, Y. Ye, Z. Huang, W. Zhang, R. Xu, P. Sayavong, S. F. Bent, J. Qin, Z. Bao, Y. Cui, *ACS Nano* **2023**, *17*, 3168–3180.

[28] P.-J. Alarco, Y. Abu-Lebdeh, A. Abouimrane, M. Armand, *Nat. Mater.* **2004**, *3*, 476–481.

[29] K. Tanaka, Y. Tago, M. Kondo, Y. Watanabe, K. Nishio, T. Hitosugi, M. Moriya, *Nano Lett.* **2020**, *20*, 8200–8204.

[30] D. Zhang, X. Meng, W. Zhang, J. Mo, Q. Zhao, B. Wang, Q. Fan, L. Liu, T. Yang, Y. Jin, R. Zhou, M. Zhang, M. Li, *Adv. Energy Mater.* **2024**, *15*, 12403565.

[31] Y. Liao, M. Zhou, L. Yuan, K. Huang, D. Wang, Y. Han, J. Meng, Y. Zhang, Z. Li, Y. Huang, *Adv. Energy Mater.* **2023**, *13*, 2301477.

[32] H. Fang, Y. Huang, W. Hu, Z. Song, X. Wei, J. Geng, Z. Jiang, H. Qu, J. Chen, F. Li, *Angew. Chem. Int. Ed.* **2024**, *63*, e202400539.

[33] Q.-W. Meng, X. Zhu, W. Xian, S. Wang, Z. Zhang, L. Zheng, Z. Dai, H. Yin, S. Ma, Q. Sun, *Proc. Natl. Acad. Sci. USA* **2024**, *121*, e2316716121.

[34] X. Ji, M. Cao, X. Fu, R. Liang, A. N. Le, Q. Zhang, M. Zhong, *Giant* **2020**, *3*, 100027.

[35] X. Ji, L.-L. Xiao, Y. Zhang, K. Yue, X. Zhou, Z.-H. Guo, *ACS Appl. Energy Mater.* **2022**, *5*, 8410–8418.

[36] C. Li, Y. Zhong, R. Liao, T. Yi, M. Zhou, R. Liu, S. Liu, D. Wu, *Adv. Mater.* **2025**, *37*, 2500142.

[37] G. Wisanrakkit, J. K. Gillham, *J. Appl. Polym. Sci.* **2003**, *41*, 2885–2929.

[38] J. P. Pascault, R. J. J. Williams, *J. Polym. Sci. Pol. Phys.* **2003**, *28*, 85–95.

[39] M. Hayashi, *Polym. J.* **2024**, *57*, 343–355.

[40] H. Ye, B. Wu, S. Sun, P. Wu, *Adv. Mater.* **2024**, *36*, 2402501.

[41] B. Yiming, Y. Han, Z. Han, X. Zhang, Y. Li, W. Lian, M. Zhang, J. Yin, T. Sun, Z. Wu, T. Li, J. Fu, Z. Jia, S. Qu, *Adv. Mater.* **2021**, *33*, 2006111.

[42] S. Han, P. Wen, H. Wang, Y. Zhou, Y. Gu, L. Zhang, Y. Shao-Horn, X. Lin, M. Chen, *Nat. Mater.* **2023**, *22*, 1515–1522.

[43] C. Feng, T. Kyu, *Electrochim. Acta* **2020**, *330*, 135320.

[44] S. H. Lee, J. Y. Hwang, S. J. Park, G. T. Park, Y. K. Sun, *Adv. Funct. Mater.* **2019**, *29*, 1902496.

[45] D. Zhang, Y. Liu, Z. Sun, Z. Liu, X. Xu, L. Xi, S. Ji, M. Zhu, J. Liu, *Angew. Chem. Int. Ed.* **2023**, *62*, e202310006.

[46] H. Wan, Z. Wang, S. Liu, B. Zhang, X. He, W. Zhang, C. Wang, *Nat. Energy* **2023**, *8*, 473–481.

[47] H. Zhang, C. Shen, Y. Huang, Z. Liu, *Appl. Surf. Sci.* **2021**, *537*, 147983.

[48] H. S. Dhattarwal, Y.-W. Chen, J.-L. Kuo, H. K. Kashyap, *J. Phys. Chem. C* **2020**, *124*, 27495–27502.

[49] T.-U. Wi, S. O. Park, S. J. Yeom, M.-H. Kim, I. Kristanto, H. Wang, S. K. Kwak, H.-W. Lee, *ACS Energy Lett.* **2023**, *8*, 2193–2200.

[50] Y. Ma, J. Wan, Y. Yang, Y. Ye, X. Xiao, D. T. Boyle, W. Burke, Z. Huang, H. Chen, Y. Cui, Z. Yu, S. T. Oyakhire, Y. Cui, *Adv. Energy Mater.* **2022**, *12*, 2103720.

[51] M. Yang, K. Yang, Y. Wu, Z. Wang, T. Ma, D. Wu, L. Yang, J. Xu, P. Lu, J. Peng, Z. Jiang, X. Zhu, Q. Gao, F. Xu, L. Chen, H. Li, F. Wu, *ACS Nano* **2024**, *18*, 16842–16852.

[52] J. Xiao, Q. Li, Y. Bi, M. Cai, B. Dunn, T. Glossmann, J. Liu, T. Osaka, R. Sugiura, B. Wu, J. Yang, J.-G. Zhang, M. S. Whittingham, *Nat. Energy* **2020**, *5*, 561–568.

[53] B. D. Adams, J. Zheng, X. Ren, W. Xu, J. G. Zhang, *Adv. Energy Mater.* **2017**, *8*, 1702097.

[54] W. Bao, Y. Zhang, L. Cao, Y. Jiang, H. Zhang, N. Zhang, Y. Liu, P. Yan, X. Wang, Y. Liu, H. Li, Y. Zhao, J. Xie, *Adv. Mater.* **2023**, *35*, 2304712.

[55] D. Bao, Y. Tao, Y. Zhong, W. Zhao, M. Peng, H. Zhang, X. Sun, *Adv. Funct. Mater.* **2023**, *33*, 2213211.

[56] X. Zhang, C. Fu, S. Cheng, C. Zhang, L. Zhang, M. Jiang, J. Wang, Y. Ma, P. Zuo, C. Du, Y. Gao, G. Yin, H. Huo, *Energy Stor. Mater.* **2023**, *56*, 121.